Macromolecules

pubs.acs.org/Macromolecules Article

Nanospheres with Patches Arranged in Polyhedrons from Self-Assembly of Solution-State Diblock Copolymers under Spherical Confinement

Jiaping Wu, Xin Wang, Zheng Wang, Yuhua Yin, Run Jiang, Yao Li,* and Baohui Li*

Cite This: *Macromolecules* 2023, 56, 335−348 Read Online

ACCESS | Metrics & More | Article Recommendations

ABSTRACT: Self-assembly of sphere-forming solution-state amphiphilic diblock copolymers under spherical nanopore confinement is investigated using a simulated annealing technique. For two types of cases of different pore−surface/copolymer interactions, sequences of self-assembled patchy nanospheres are obtained, and phase diagrams are constructed. Self-assembled patchy nanospheres with 1−21 solvophobic domains are observed. The outermost solvophobic domains (patches) are packed into various polyhedrons when their number is larger than 3, where three Platonic solids of a regular tetrahedron, an octahedron, and an icosahedron and seven Johnson solids of J12, J13, J17, J50, J51, J86, and J87 are identified. In addition, another Johnson solid of J84 is identified in a structure with two categories of B-domains. These polyhedrons have all or most of their faces in a triangular shape, and hence, they are closer to spherical in shape, which may relieve the chain stretching. Nanospheres with 1, 4, 6, 9, and 12 numbers of patches occur in relatively large windows in the phase diagrams of both types of cases. In one of the two types of cases, all nanospheres with any number of 1−14 patches occur in the phase diagram, whereas in the other type of cases, nanospheres with 2, 3, 5, 11, and 13 numbers of patches are absent in the phase diagram. Furthermore, at a given pore size, the number of patches changes nonmonotonically or is unchanged with an increase in the strength of the pore−surface/copolymer interactions for one type or the other type of case, respectively. Quantitative calculations are performed to elucidate mechanisms of the window size in the phase diagrams of nanospheres with different numbers of patches and structure details. All the observed phase behaviors can be well-explained based on the structure frustration, the conclusion being that the systems tend to avoid forming polyhedral structures with uneven distribution of solvophobic domains, and the differences between the two types of cases. Our results may provide a fundamental understanding of the relationship among confinement conditions, solvent conditions, and self-assembled structures.

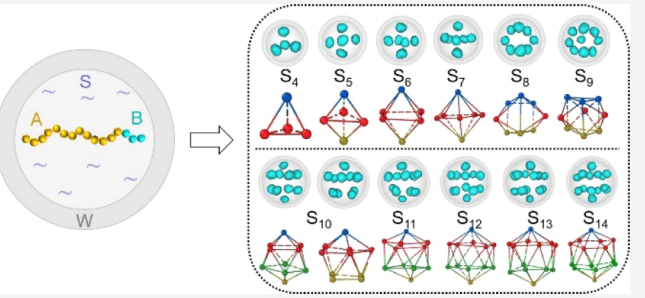

1. INTRODUCTION

Block copolymers can self-assemble into phase-separated periodic nanostructures, such as lamellae, gyroid, cylinders, spheres, and have attracted much scientific interest due to the potential application of these structures in various areas,[1−4] such as in nanolithography[3] and material science.[4] Confinement can be used to break the symmetry of structures formed in the self-assembly of block copolymers and hence generate novel structures that cannot be obtained in bulk.[3,5,6] In general, confinement can be classified into one-dimensional (1D) planar confinement,[3,7−10] two-dimensional (2D) cylindrical confinement,[5,11−16] and three-dimensional (3D) spherical confinement[6,17−21] based on the confining geometries. Previous extensive studies showed that frustration induced by 1D confinement of block copolymers in thin films can lead to different orientations and adjustable periods of structures depending on the surface−block interactions and film thickness,[22,23] while 2D cylindrical confinement and 3D spherical confinement could induce frustration and distortions that cannot be observed in bulk or 1D confinement due to the curvature of the confining pore. Moreover, a large number of novel and frustrated structures were found,[5,9,20,24−27] such as cylindrical (spherical)−concentric lamellar structures and stacked lamellae, as well as nonlamellar structures[20,27] including Janus-type, tennis-ball-, mushroom-, wheel-, or screw-like structures[20] for the bulk lamella-forming diblock copolymers, while for the bulk cylinder-forming diblock copolymers, single helices, double helices, triple helices,

Received: October 21, 2022
Revised: December 12, 2022
Published: December 29, 2022

https://doi.org/10.1021/acs.macromol.2c02166
Macromolecules 2023, 56, 335−348

stacked toroid structures,[5,15,28−30] or curved cylinders[9,24,27] were observed in cylindrical or spherical pore confinement.

The self-assembly of sphere-forming diblock copolymers confined in 3D spherical nanopores also attracts much scientific attention. Thirty years ago, Reffner experimentally observed irregularly packed spheres when sphere-forming diblock copolymers were confined in droplets and heated to remove solvent.[24] Various patchy nanoparticles were observed experimentally and predicted with simulations from self-assembly of diblock copolymers under emulsion solvent evaporation-induced 3D soft confinement,[31−36] where the packing of the patches presents some symmetry when the number of patches is small.[31] Recently, Zhao et al. studied the phase behavior of both bulk cylinder-forming and sphere-forming diblock copolymers confined in the spherical pores using the self-consistent field theory.[37] They constructed a phase diagram as a function of the pore radius and the volume fraction of the copolymer and found a variety of interesting polyhedral shapes formed by the packing of spherical domains with the numbers from 4 to 12. Furthermore, the number of spherical domains changes discontinuously with an increase in the pore size, and structures with higher symmetry have a larger stable region in the phase diagram.[37] The packing of spherical particles is an ancient and intriguing issue.[38] Related studies, including the packing of a small number of colloidal microspheres fabricated from cross-linked PS in a cluster using oil-in-water emulsion and solvent evaporation[39] and the packing of a small number of hydrophobic nanoparticles confined in micelles formed by amphiphilic diblock copolymers,[40] were studied.

Compared to the melt system, sphere-forming block copolymer solution should be easier to obtain by choosing various selective solvents, just like that observed for the unconfined system previously.[41] The self-assembly behaviors of the 3D-confined sphere-forming block copolymer in the presence of a solvent, rather than when the solvent evaporated, are much less understood. Previous experimental studies of 2D confinement of block copolymer solutions showed that the dimensions of the nanochannels not only control the packing of spherical micelles but also affect the shape/morphology of individual micelles,[42] although the arrangement of spherical micelles in that solution system is similar to that of spherical domains obtained in the block copolymer melt under the same 2D confinement.[15]

In the present work, we study the effect of 3D confinement on the self-assembly of sphere-forming amphiphilic diblock copolymer solutions using a simulated annealing technique. The 3D confinement is realized by putting diblock copolymer solutions into a spherical nanopore. Patchy nanospheres with various numbers of solvophobic domains are obtained and phase diagrams are constructed as a function of the pore radius and the surface−block interaction. Quantitative calculations are performed to elucidate the mechanisms of the window size in the phase diagrams of nanospheres with different numbers of patches and details of structures. The effects of the polymer segment concentration on the self-assembled patchy nanospheres and structural details are further investigated. Our simulation results are compared with previous related studies.

2. MODEL AND METHOD

The solution-state AB diblock copolymers are modeled by the single-site bond fluctuation model[43−45] and the simulations are performed using the simulated annealing method.[46,47] The details of the model and method can be found elsewhere.[48] Asymmetric AB diblock copolymer model molecules of the form $A_{13}B_3$ are used in the study, that is, the degree of polymerization of each A- and B-block is $N_A = 13$ and $N_B = 3$. The volume fraction of B-block is $f_B \equiv N_B/N = 0.1875$, where $N \equiv N_A + N_B = 16$ is the total degree of polymerization of each AB diblock copolymer molecule. In our study, the AB diblock copolymers are dissolved in solution and confined in a spherical nanopore of radius R. The pore is embedded in a simple cubic lattice of volume $V = L^3$ with L being larger than $2R$. The segment concentration is defined as $C_p \equiv nN/V_p$, with n being the number of the model molecules and V_p the total number of lattice sites inside the pore. The model molecules are assumed to be self-avoiding and mutually avoiding in all the simulation processes. The bond lengths between two consecutive segments in a copolymer molecule are set to be 1 and $\sqrt{2}$, and thus, each site has 18 nearest-neighbor sites. The starting configuration is generated by putting the desired number of model molecules on the lattice sites inside the pore randomly to reach the desired C_p value. Only the nearest-neighboring interactions are considered and modeled by assigning energy, $E_{ij} = \varepsilon_{ij}k_BT_{ref}$, to each nearest-neighboring pair of unlike components i and j, where i, j is A, B, S, and W with S being the solvent molecules and W the lattice sites on the pore wall (surface); ε_{ij} is the reduced interaction energy; k_B is the Boltzmann constant; and T_{ref} is the reference temperature. A-blocks and B-blocks are incompatible, so the A−B interactions are set to be $\varepsilon_{AB} = 1.0$. A-blocks are solvophilic, while B-blocks are solvophobic; hence, the A−S and B−S interactions are set to be $\varepsilon_{AS} = -0.5$ and $\varepsilon_{BS} = 0.5$. The solvent−pore surface interactions are set to be 0. For a given C_p, two types of cases are studied with the only difference in A-surface interactions: (α) $\varepsilon_{AW} = -\varepsilon_{BW}$ and (β) $\varepsilon_{AW} = 0.0$, and ε_{BW} is varied from 0 to 4.0 with a step of 0.5 for phase diagrams in both types of α and β cases. The initial temperature is set as $T_0 = 100T_{ref}$, and the annealing schedule and the sampling strategy are the same as those used previously.[27] Under a given set of parameters, 50 to 100 simulations are performed with the only difference being in the random number generator seed. If multiple structures are obtained in our simulations under the given set of parameters, structures with the highest probability of occurrence are called frequently occurring structures, while others are called less frequently occurring structures.

Some quantities are calculated in the study to characterize the details of the structures. The radial density profiles of I-segments $P_I(r)$ (I = A, B) in the confining pore are calculated with $P_I(r) = n_I(r)/M(r)$, with $n_I(r)$ and $M(r)$ being the number of I-segments and the number of lattice sites in the spherical shell of thickness 1 at a distance r from the pore center, respectively. The index of polydispersity of the edge length of a polyhedron is defined as $pdi_{edge} \equiv E(L_{edge}^2)/E^2(L_{edge})$, where L_{edge} is the length of each edge in the polyhedron formed by packing of B-domains in the self-assembled structures and $E(L_{edge})$ and $E(L_{edge}^2)$ are the average values of L_{edge} and L_{edge}^2, respectively, in a polyhedron. Similarly, the index of polydispersity of the size of each B-domain is defined as $pdi_{size} \equiv E(n_B^2)/E^2(n_B)$, where n_B is the number of B-segments inside each B-domain and $E(n_B)$ and $E(n_B^2)$ are the average values of n_B and n_B^2, respectively, in a system. $pdi_{size} = 1$ if all the B-domains have the same n_B value, while pdi_{size} gets larger if the difference between the n_B values of the B-domains gets larger. The nonsphericity of an aggregate or a collection of particles is

https://doi.org/10.1021/acs.macromol.2c02166
Macromolecules 2023, 56, 335−348

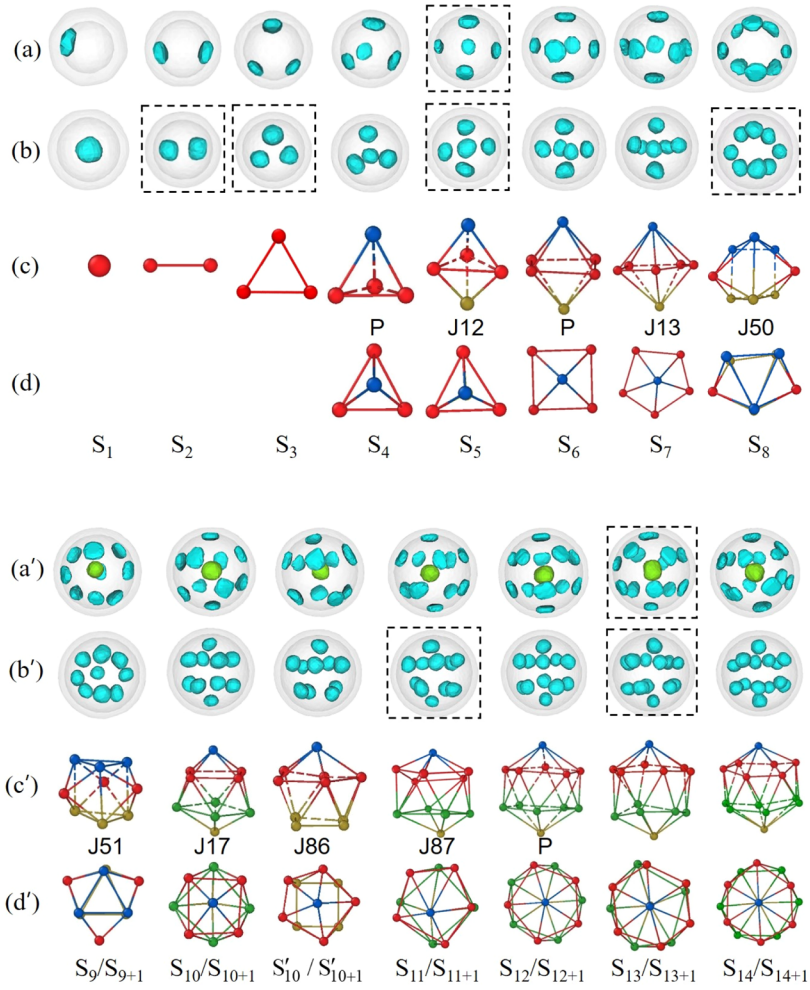

Figure 1. Typical snapshots of structures obtained at (a,a′) $\varepsilon_{AW} = \varepsilon_{BW} = 0$ and (b,b′) $-\varepsilon_{AW} = \varepsilon_{BW} = 1.0$. In (a,a′,b,b′), isosurface contour plots of only B-domains are shown. Structures S_1 to S_{14}/S_{14+1} are obtained at pore radius R = 4, 6, 7, 8, 9, 10, 11, 11, 12, 13, 13, 14, 15, and 15, respectively, in (a,a′) and at R = 8, 9, 9, 10, 10, 11, 12, 13, 13, 14, 14, 15, 16, and 16, respectively, in (b,b′). In (a,a′,b,b′), the outermost B-domains are shown in blue, while the B-domain at the pore center is in green color. Each dot in (c, d) and (c', d') corresponds to the center of a B-domain shown in (b) and (b'), respectively, and lines are added to guide the eyes, where the dots and lines are assigned to different colors for clarity. Snapshots in (c) and (d) and in (c') and (d') are viewed in two perpendicular directions. Less frequently occurring structures are labeled by framing the snapshots with dashed lines in (a,b,a′,b′).

defined as[49,50] $\kappa \equiv 3(\lambda_x^4 + \lambda_y^4 + \lambda_z^4)/2(\lambda_x^2 + \lambda_y^2 + \lambda_z^2)^2 - 1/2$, where λ_x, λ_y, and λ_z are the three principal moments of the gyration tensor of the aggregate. $\kappa \in [0,1]$, $\kappa = 0$ if the aggregate is a perfect sphere and $\kappa = 1$ if all the particles in the aggregate are on a line. The normalized mean-square end-to-end distance of chains of length N is calculated as $R_e^2 = R_{e,1}^2/R_{e,0}^2$, where $R_{e,1}^2$ and $R_{e,0}^2$ are the mean-square end-to-end distance of the chains and that of the corresponding ideal chain, respectively, and $R_{e,0}^2 = b^2(N-1)$, with b being the root mean square of bond length ($b = \sqrt{5/3}$ in our model).

3. RESULTS AND DISCUSSION

In this section, we present our simulation results of structures self-assembled from an amphiphilic diblock copolymer $A_{13}B_3$ solution confined in a spherical nanopore, where the A-blocks are solvophilic and the B-blocks are solvophobic, and the reduced interactions used are $\varepsilon_{AB} = 1.0$, $\varepsilon_{AS} = -0.5$, and $\varepsilon_{BS} = 0.5$. Without confinement, our simulation results show that the model system forms a cylindrical structure, a spherical structure, and a spherical micellar morphology at segment concentrations of $C_p \geq 0.95$, $C_p = 0.2-0.85$, and $C_p < 0.2$, respectively, with the solvophobic B-blocks forming cylinders, spheres, and micelle cores due to the smaller volume fraction and the solvophobic nature of B-blocks. Under the confinement of a spherical pore, nanospheres with various numbers of B-domains are obtained when $0.1 \leq C_p \leq 0.7$. At a fixed concentration of $C_p = 0.45$, snapshots for typical structures are presented (Figures 1−3). For two types of cases of different polymer−surface interactions, phase diagrams (Figure 4) as a function of the pore radius R and interactions between the polymer and pore surface are constructed. Typical quantities include the radial density profiles of copolymer segments, the polydispersity index of the edge length in the polyhedrons formed by packing of B-domains in the self-assembled structures, the polydispersity index of the size and non-sphericity of each B-domain, and the normalized mean-square end-to-end distance of chains (Figures 5 and 6). The influence of C_p on self-assembled structures and typical quantities is presented in Figure 7.

3.1. Nanospheres with Patches in Polyhedral Structures. Figure 1 shows the variation in typical snapshots of patchy nanospheres self-assembled from the model

https://doi.org/10.1021/acs.macromol.2c02166
Macromolecules 2023, 56, 335−348

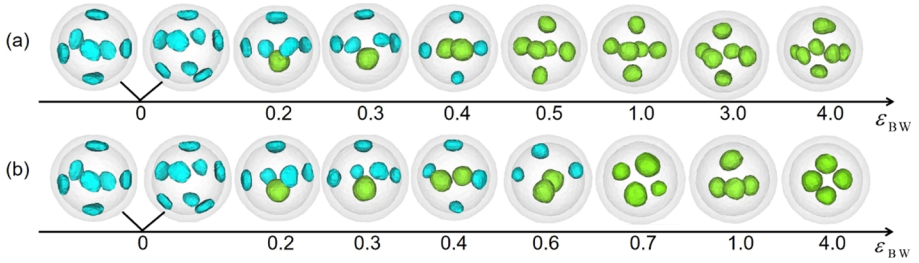

Figure 2. Typical snapshots of self-assembled structures as a function of ε_{BW} for the model system in the pore of radius R = 11, and the A-surface interaction: (a) $\varepsilon_{AW} = -\varepsilon_{BW}$ and (b) $\varepsilon_{AW} = 0$. The B-domains attached to the pore surface and away from the surface are shown in blue and green colors, respectively.

amphiphilic diblock copolymers in solution confined in a spherical nanopore of pore radius R for two cases of different surface−copolymer interactions. In Figure 1, each structure is named S_i or S_{i+1} with i (=1, ..., 14) being the number of solvophobic B-domains nearest to the pore surface (outermost B-domains or patches) and the "i + 1" indicating that besides the i patches, there is one B-domain located at the pore center. As shown in Figure 1a,a′, for the case of energetically neutral surfaces ($\varepsilon_{AW} = \varepsilon_{BW} = 0$), the i patches in a structure S_i/S_{i+1} are all attached to the pore surface, which is due to the following two reasons. One reason is the entropy-driven attraction of the minority B-blocks to the neutral surfaces,[23,51] and the other one is the resulting favorable energy when the patches are attached to the pore surface since the increased contact between B-segments and the pore surface can reduce the unfavorable contact between A- and B-segments and that between B-segments and solvents. It is noted that each of the patches is in a nearly convex lens shape (not a spherical shape), whereas the B-domain located at the pore center is in a spherical shape. For the sake of clarity, the B-domain located at the pore center in Figure 1a′ is shown in green color. When the nature of the pore surface changes to be attractive to the majority A-blocks while repulsive to the minority B-blocks ($-\varepsilon_{AW} = \varepsilon_{BW} = 1.0$), all B-domains are of nearly spherical shape and are away from the pore surface, as shown in Figure 1b,b′. A common feature for structures shown in Figure 1a,a′,b,b′ is that the packing of the patches is the same when the number of patches is the same regardless of whether there is a B-domain located at the pore center or not or whether the patches are attached to the pore surface or not. Therefore, in the following, we will describe structures S_i and S_{i+1} together.

As shown in Figure 1, the B-domain in structure S_1 is located at the pore center, the two B-domains in structure S_2 are located at the two poles (two sides) of the pore, and the three B-centers (the center of each B-domain is abbreviated as B-center hereafter) in structure S_3 constitute an approximate regular triangle. For structures S_i/S_{i+1} with $4 \le i \le 14$, the B-domains are packed into polyhedrons having an apparent high symmetry, as shown in Figure 1c,d,c′,d′. Among these polyhedrons, three of the five Platonic solids[52] (or convex, regular polyhedrons) are identified as shown in Figure 1 (labeled with "P"), that is, a regular tetrahedron (S_4), a regular octahedron (S_6), and a regular icosahedron (S_{12}); and seven Johnson solids[52,53] are identified in the other polyhedral structures, that is, structure S_5 is the triangular bipyramid (J12), S_7 is the pentagonal bipyramid (J13), S_8 is the biaugmented triangular prism (J50), S_9 is the triaugmented triangular prism (J51), S_{10} corresponds to two degenerate structures of the gyroelongated square bipyramid (J17) and the sphenocorona (J86) (to distinguish these two structures, the structure corresponding to J86 is called S_{10}'), and S_{11} is the augmented sphenocorona (J87). Structure S_{14} is the gyroelongated hexagonal bipyramid and together with the gyroelongated square bipyramid (S_{10}) and the gyroelongated pentagonal bipyramid (S_{12}) belongs to the gyroelongated bipyramid constructed by elongating an n-gonal bipyramid by inserting an n-gonal antiprism between its congruent halves.

It is interesting to find that the three Platonic solids identified in our simulations have all their faces in a triangular shape. Furthermore, the seven Johnson solids identified in our simulations have all (J12, J13, J17, and J51) or most of their faces (except only one or two tetragonal faces in J50 and J87, or J86, respectively) in a triangular shape; although there are 92 Johnson solids[53] in total and each of them can be with faces in a triangle, a tetragon, a pentagon, a hexagon, an octagon, or a decagon, and the whole shape of a Johnson solid can be close to or quite deviating from a sphere. Thus, we conclude that polyhedrons prefer triangular faces. The reason is that for a fixed B-domain number, triangular faces will make the polyhedron have more faces than that with other shaped faces (such as tetragonal or other polygonal shapes). Therefore, under a fixed number of vertices, a polyhedron with more triangular faces is closer to a sphere in shape than that with more other-shaped faces, which may relieve the chain stretching.

It is also interesting to find that the B-centers are usually distributed into layers. The B-centers in structures S_5, S_6, or S_7 are distributed into three layers with the number of B-domains in each layer being [1, n, 1], with n = 3, 4, and 5 in S_5, S_6, and S_7, respectively, as shown in Figure 1c. However, the B-centers in structures S_{10}, S_{11}, S_{12}, S_{13}, or S_{14} are distributed into four layers with the number of B-domains in each layer being [1, n, m, 1], where [n, m] = [4,4], [5,4], [5,5], [6,5], and [6,6] in structures S_{10}, S_{11}, S_{12}, S_{13}, and S_{14}, respectively, as shown in Figure 1c′. Structure S_{10}' can be regarded as formed by deleting the B-center located at the side of the layer having four B-centers in S_{11}. Structure S_9 can be constructed by attaching an equilateral square pyramid to each of the three square faces of a triangular prism, whereas structure S_8 can be regarded as constructed by randomly deleting an equilateral square pyramid in S_9. For structures with the outermost B-domain number being larger than 14, we find that the B-domains are still packed into polyhedrons with most of their faces being in a triangular shape. These polyhedrons, however, are without apparent symmetry.

Snapshots shown in Figure 1 include both frequently and less frequently occurring structures, where each less frequently occurring structure is framed by dashed lines. It is noted that

https://doi.org/10.1021/acs.macromol.2c02166
Macromolecules 2023, 56, 335−348

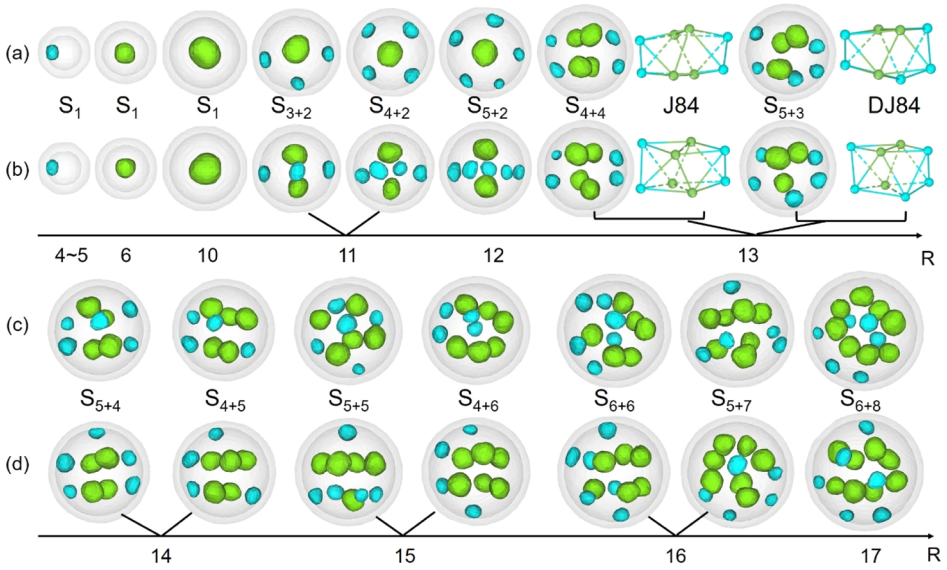

Figure 3. Typical snapshots of self-assembled structures as a function of R for systems with block−surface interactions being $\varepsilon_{AW} = 0$ and $\varepsilon_{BW} = 0.5$. (a) and (b) and (c) and (d) are viewed from two different directions. The B-domains attached to the pore surface and away from the surface are shown in blue and green colors, respectively. For structures S_{4+4} and S_{5+3} formed at $R = 13$, lines are shown to illustrate the structures J84 and DJ84.

structures S_5 and S_{13} are less frequently occurring in both cases, and structures S_2, S_3, S_8, and S_{11} are less frequently occurring in the case of $-\varepsilon_{AW} = \varepsilon_{BW} = 1$, whereas they are frequently occurring in the case of $\varepsilon_{AW} = \varepsilon_{BW} = 0$. These results indicate that the occurrence frequency of some structures depends on the polymer−pore surface interactions, and the influence of the interactions on the self-assembled structures is further investigated.

Typical snapshots of self-assembled structures as a function of ε_{BW} at a fixed pore radius of $R = 11$ are shown in Figure 2 to illustrate the effect of the pore surface interactions on the self-assembled structures. Here, results are presented for two types of cases with the only difference being in ε_{AW}, that is, $\varepsilon_{AW} = -\varepsilon_{BW}$ in the type α case while $\varepsilon_{AW} = 0$ in the type β case. It is noted that the B-domains in snapshots shown in Figure 2 can be classified into two categories according to the domain shape and position. For the sake of clarity, we name the B-domains being in nearly lens shape and attached to the pore surface (in blue color in Figure 2) as category 1 and those being in a spherical shape and far away from the pore surface (in green color) as category 2. As shown in Figure 2a, for the type α case, the total number of B-domains and the number belonging to category 1 or 2 change with increasing ε_{BW} in the following way: seven or eight B-domains all belonging to category 1 at $\varepsilon_{BW} = 0$ → six B-domains with five of them belonging to category 1 while the other one to category 2 at $\varepsilon_{BW} = 0.2$−0.3 → six B-domains with four of them belonging to category 1 while the other two to category 2 at $\varepsilon_{BW} = 0.4$ → six and seven B-domains all belonging to category 2 at $\varepsilon_{BW} = 0.5$−3.0 and $\varepsilon_{BW} = 4.0$, respectively. That is, the number of the B-domains shows a nonmonotonic change with ε_{BW}. In the type β case, as shown in Figure 2b, the variations in the domain number and shape with ε_{BW} are just like those in the type α case when $\varepsilon_{BW} = 0$−0.4. However, the number of B-domains continues to decrease to five and further to four when increasing ε_{BW} to $\varepsilon_{BW} = 0.6$ and further to $\varepsilon_{BW} \geq 0.7$.

It is noted that B-domains belonging to the two categories may simultaneously occur in one system at $\varepsilon_{BW} = 0.2$−0.4 in Figure 2a and $\varepsilon_{BW} = 0.2$−0.6 in Figure 2b. For these structures with two categories of B-domains, we name them S_{i+j}, with i and j being the number of the outermost and inner B-domains, respectively. Our further results show that such structures may also occur at other pore radii when ε_{BW} is at the above-mentioned regions. Figure 3 shows typical snapshots of structures obtained in the type β case at $\varepsilon_{AW} = 0$ and $\varepsilon_{BW} = 0.5$ as a function of pore radius R. As shown in Figure 3, with increasing R, the structure changes from S_1 ($R = 4$−10) → S_{3+2}/S_{4+2} ($R = 11$) → S_{5+2} ($R = 12$) → S_{4+4}/S_{5+3}($R = 13$) → S_{5+4}/S_{4+5} ($R = 14$) → S_{5+5}/S_{4+6} ($R = 15$) → S_{6+6}/S_{5+7} ($R = 16$) → S_{6+8} ($R = 17$). At a very small pore radius of $R = 4$−10, only one B-domain is formed in the system. It is interesting to notice that the B-domain is attached to the pore surface when $R = 4$−5, while it is located at the pore center when $R = 6$−10. With increasing R, the total number of B-domains increases and B-domains belonging to the two categories (in blue and green colors) coexist in each system. With the increase in R from 11 to 17, the number of B-domains away from the surface (in green color) increases from 2 → 3 or 4 → 4 or 5 → 5 or 6 → 6 or 7 → 8. It should be mentioned that the structures S_{i+j} (with $j > 1$) shown in Figure 3 are different from the structures S_k or S_{k+1} shown in Figure 1 even when $k = i + j$. For example, structure S_{4+2} is different from structure S_6. Furthermore, a polyhedron formed by packing of the B-domains in structure S_{i+j} is usually without apparent symmetry due to the different distances from the B-centers belonging to two categories to the pore center. However, we do observe a polyhedron with apparent symmetry formed in structure S_{4+4}; it is the triangular dodecahedron belonging to the Johnson solid J84, as shown in Figure 3 at $R = 13$. Structure J84 has eight vertices, four of which are farther from the pore center than the other four, and the B-centers in structure S_{4+4} just meet such a condition. On the other hand, the eight B-centers in structure S_8, being of the same category and the same distances to the pore center, cannot meet the condition of forming J84, which is the reason that J84 is not observed in structure S_8. Structure S_{5+3}, observed at $R = 13$ as a degenerate structure with S_{4+4}, is identified as a deformed J84, here called DJ84. Our simulation results show that structures S_{i+j} obtained in the type α case at

https://doi.org/10.1021/acs.macromol.2c02166
Macromolecules 2023, 56, 335−348

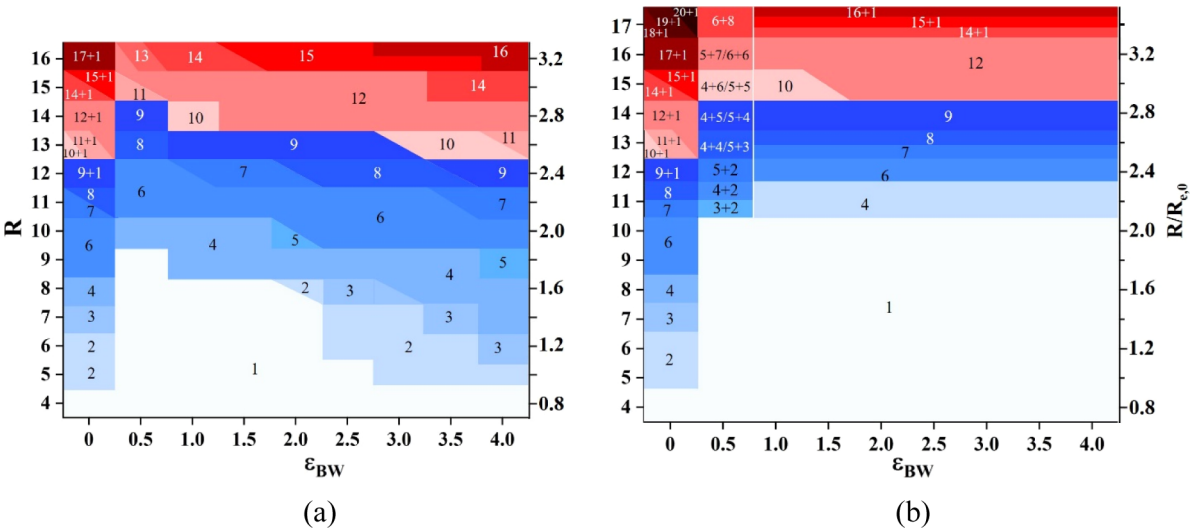

Figure 4. Phase diagrams showing the number of solvophobic B-domains in the frequently occurring structures as a function of the pore radius R (or $R/R_{e,0}$, where $R_{e,0}$ is the root of the mean-square end-to-end distance of the corresponding ideal chain) and the interaction parameter ε_{BW} in a step of 0.5. The corresponding typical structures are shown in Figures 1−3. The A-surface interactions are $\varepsilon_{AW} = -\varepsilon_{BW}$ in (a) and $\varepsilon_{AW} = 0$ in (b). To clarify, the background color varies from light blue to dark blue to light red and further to dark red, showing that the number of B-domains varies from small to large.

$-\varepsilon_{BW} = \varepsilon_{BW} = 0.4$ are similar to those obtained in the type β case shown in Figure 3.

The occurrence of two categories of B-domains in one system can be understood based on the following analysis. When the pore surface is neutral to the two blocks ($\varepsilon_{AW} = \varepsilon_{BW} = 0$), the B-domains are attached to the pore surface due to the two reasons mentioned earlier. Thus, these two reasons induce a tendency (called "the first tendency") to drive the B-domains attached to the pore surface. With increasing ε_{BW}, the repulsive interaction between the B-segments and the pore surface tends to drive the B-domains away from the pore surface (called "the second tendency"). Hence, all the B-domains can be away from the pore surface only when ε_{BW} is large enough so that the second tendency can offset or be stronger than the first tendency. From Figure 2, it is noted that all the B-domains are away from the pore surface at $\varepsilon_{BW} = 0.5$ and 0.7 for the type α and β cases, respectively; while when $0 < \varepsilon_{BW} < 0.5$ (or $0 < \varepsilon_{BW} < 0.7$) for the type α (or β) case, balancing between the two tendencies results in various structures with some B-domains attached to the pore surface while others away from the pore surface. This is the reason why two categories of B-domains are formed in a system with more than one B-domains, which is consistent with those shown in Figure 3. On the other hand, at a given ε_{BW} value, the interactions of $\varepsilon_{AW} = -\varepsilon_{BW}$ used in the type α case are equivalent to a stronger surface selectivity than that used in the type β case of $\varepsilon_{AW} = 0$, which is the reason that a relatively smaller ε_{BW} value is needed in the type α case to force all the B-domains away from the pore surface than that needed in the type β case. In a small pore, the amount of block copolymers in the system is small, and hence, only one B-domain is formed and the position of this B-domain can be deduced based on the following analysis. At $R = 4-5$, the amount of block copolymers in the system is very small, and hence, only one small B-domain is formed, while R is much smaller than the length of the solvophilic A-block, and hence, the small B-domain is attached to the pore surface so that the A-blocks can have a relatively large space with less compression. In this case, the punishment due to the repulsive interaction between the pore surface and B-blocks can be offset by the reduced entropy loss due to the less compression of A-blocks. When $R = 6$, the amount of block copolymers in the system is about 2 times that when $R = 5$. In this case, the system may form one big B-domain or two smaller B-domains. If the system forms two smaller B-domains, the locations of them would be in one of the following three patterns: (1) both of them are attached to the pore surface, that is, the structure S_2 shown in Figure 1a; (2) both of them are away from the pore surface, that is, the structure S_2 shown in Figure 1b; and (3) one of them is attached to the pore surface, while the other is away from the pore surface. Pattern (1) would result in high energy due to the increased contact area between the B-segment and the pore surface, while patterns (2) and (3) mean that the distance between the two B-domains is less than the pore diameter, and when the size of each B-domain is considered, the space left for A-blocks from one B-center in the direction of connecting the two B-centers is much less than R, which would result in strongly compressed A-blocks. On the other hand, the system may form one big B-domain. In this case, if the B-domain is attached to the pore surface, the A-blocks emitting from the surface of the B-domain would be too crowded since the A-blocks are only distributed at the inner side of the B-domain surface (the outer side is attached to the pore surface). The crowded distribution of A-segments reduces the contact between A-segments and solvent, and hence, it is energetically unfavorable. On the other hand, if the big B-domain is located at the pore center, it can remove the contact between the B-segment and pore surface and can have relatively large space for A-blocks from every direction; therefore, it is the best choice in this case for a system with $R = 6$. For systems with $R = 7-10$, the amount of block copolymers in the system is about 2−8 times that when $R = 5$. In this case, the system may form one big B-domain or several smaller B-domains. On the basis of an analysis such as that for the system with $R = 6$, it can also be deduced that forming one big B-domain located at the pore center is the best choice for these systems. As the pore is further larger to $R = 11$, if the system remains forming one big B-domain located at the pore center, the stretching of both B-blocks and A-blocks will be

https://doi.org/10.1021/acs.macromol.2c02166
Macromolecules 2023, 56, 335−348

strong, which is entropically unfavorable. Moreover, simultaneously A-blocks would be much more crowded near the B-domain surface, which will reduce the contact between A-segments and solvent. Hence, forming one big B-domain is energetically unfavorable at $R = 11$, as analyzed above. On the other hand, if the system forms several smaller B-domains with some of them being attached to the pore surface while others being away from the pore surface, the space may be allocated effectively so that the stretching of both B-blocks and A-blocks, as well as the crowding of A-blocks, are all relieved; being favorable for both entropic and energetic sides, which can offset the punishment due to the increased unfavorable contact between the B-segments and the pore surface. This is the case as shown in Figure 3.

It is also noted that structures with two or three B-domains are absent in the structure sequence shown in Figure 3. The above analysis indicates that the distribution of the two or three B-domains inside the spherical space would result in high energy if all of them are attached to the pore surface, or result in strongly compressed A-blocks if one or two of them are away from the pore surface. These analyses also apply to the systems with $-\varepsilon_{AW} = \varepsilon_{BW} = 1$ for which structures are shown in Figure 1b. In this case, the value of ε_{BW} is larger so that patterns (1) and (3) mentioned above would result in high energy, while pattern (2) would result in strongly compressed A-blocks. That is, the structure frustration hinders the occurrence of structures S_2 and S_3 as frequently occurring structures in Figure 1b. On the other hand, for systems with $\varepsilon_{AW} = \varepsilon_{BW} = 0$, pattern (1) would reduce the entropy loss and not result in high energy, and hence, it is the best choice, which is consistent with the result shown in Figure 1a.

3.2. Phase Diagrams. We further construct two-phase diagrams as shown in Figure 4a,b for the type α and β cases, respectively, for the window size of frequently occurring structures S_i and S_{i+j} as a function of the pore radius R and the interaction strength of the pore surface with B-blocks ε_{BW}. Note that the two types of cases are the same at $\varepsilon_{AW} = \varepsilon_{BW} = 0$ (neutral surface), and similar structures including two categories of B-domains are obtained when ε_{BW} is at $\varepsilon_{BW} = 0.2-0.4$ and at $\varepsilon_{BW} = 0.2-0.6$, as shown in Figure 2a,b, respectively. Thus, we now focus on the different phase behavior between the two types of cases when each system forms only one category of B-domains, which are away from the pore surface, that is, when $\varepsilon_{BW} \geq 0.5$ in the type α case and $\varepsilon_{BW} \geq 1.0$ in the type β case. As the polyhedrons formed from structures S_i with $i \geq 15$ do not have apparent symmetry, we mainly focus on structures S_1-S_{14} in the phase diagram, where three main differences between the two types of cases are found, as listed in the followings:

(1) As shown in Figure 4a for the type α case, with increasing R and ε_{BW}, each of the structures S_1-S_{14} occurs in the phase diagram although the window of some structures is very small. It should be noted that the less frequently occurring structures, as shown in Figure 1, are frequently occurring at other interaction strengths, as shown in the phase diagram in Figure 4a. The structures with the window size ranked from the largest to the smallest are approximately in the following order: S_1, S_4, S_6, S_9, $S_{12} \rightarrow S_2$, S_3, S_7, S_8, $S_{10} \rightarrow S_5$, S_{11}, $S_{14} \rightarrow S_{13}$. It is noted that structures S_1, S_4, S_6, S_9, and S_{12} occur in the whole ε_{BW} range, while other structures only occur at some ε_{BW} values. As shown in Figure 4b for the type β case, structures S_1, S_4, S_6, S_7, S_8, S_9, S_{12}, and S_{14} occur when $\varepsilon_{BW} \geq 1.0$, and structure S_{10} occurs only when $1.0 \leq \varepsilon_{BW} \leq 1.5$, while structures S_2, S_3, S_5, S_{11}, and S_{13} do not occur when $\varepsilon_{BW} \geq 1.0$. It is obvious that the frequently occurring structures in the type α case are much richer than those in the type β case. On the other hand, it is noted that structures S_1, S_4, S_6, S_9, and S_{12} occur in relatively larger windows in the diagram, which is the same as that in the type α case. It is interesting to notice that these structures of relatively larger windows correspond to the three identified Platonic solids of a regular tetrahedron (S_4), an octahedron (S_6), and an icosahedron (S_{12}) and one Johnson solid of J51 (S_9).

(2) In the type α case, a nonmonotonic change in the number of B-domains in the observed structures is found when ε_{BW} is increased from 0 to 4.0 at a fixed pore radius R, for example, the sequences of $S_3 \rightarrow S_1 \rightarrow S_2 \rightarrow S_3 \rightarrow S_4$, $S_6 \rightarrow S_4 \rightarrow S_5 \rightarrow S_6$, and $S_{12+1} \rightarrow S_9 \rightarrow S_{10} \rightarrow S_{12}$ are found when fixing the value of R at 7, 10, and 14, respectively. That is, at a given R, the number of the B-domains has a minimum value at $\varepsilon_{BW} \approx 0.5$, and after that minimum value, it increases with ε_{BW} in the listed ε_{BW} range. However, in the type β case, at a fixed R, the number of the B-domains also decreases from $\varepsilon_{BW} = 0$ to 0.7, whereas it remains almost unchanged with a further increase in ε_{BW} when $\varepsilon_{BW} \geq 1.0$. This could be understood by the difference in the ε_{AW} value used in the type α and β cases. As mentioned earlier, all the B-domains are away from the pore surface at $\varepsilon_{BW} = 0.5$ and 0.7 for the type α and β cases, respectively. On the other hand, upon further increasing ε_{BW}, the attractions between the pore surface and A-blocks are strengthened in the type α case, and hence, A-blocks tend to be near the pore surface. Forming more B-domains favors the contact between the A-segment and pore surface, and it is energetically favorable in the type α case. Hence, the number of B-domains increases with ε_{BW} when $\varepsilon_{BW} > 0.5$. On the other hand, when $\varepsilon_{BW} = 0$, B-domains tend to be near the pore surface due to the entropy-driven attraction of the shorter B-blocks to the neutral surfaces,[23,51] thus forming more B-domains, which favors the contact between the B-segment and pore surface, and it is entropically favorable. Therefore, the number of B-domains at $\varepsilon_{BW} = 0$ is larger than that at $\varepsilon_{BW} = 0.5$. The above reasons result in the nonmonotonic change in the number of the B-domains with ε_{BW} in the observed structures at a fixing R in the type α case. However, in the type β case, the value of ε_{AW} is always fixed at 0. When ε_{BW} is large enough, that is, $\varepsilon_{BW} \geq 1.0$, further increasing ε_{BW} would not affect the behavior of B-blocks since the pore surface and B-domains are separated by A-blocks and solvent. Therefore, the number of B-domains remains almost unchanged with increasing ε_{BW} when $\varepsilon_{BW} \geq 1.0$ at a fixed R in the type β case.

(3) In the type β case, to form a structure with the same number of B-domains as that in the type α case, a larger pore radius R is needed. For example, structure S_4 appears at $R = 7-10$ depending on ε_{BW} in the type α case, while it appears at a larger pore radius of $R = 11$ in the type β case. This indicates that the effective pore radius for the outermost B-domains should be different in the studied two types of cases.

https://doi.org/10.1021/acs.macromol.2c02166
Macromolecules 2023, 56, 335−348

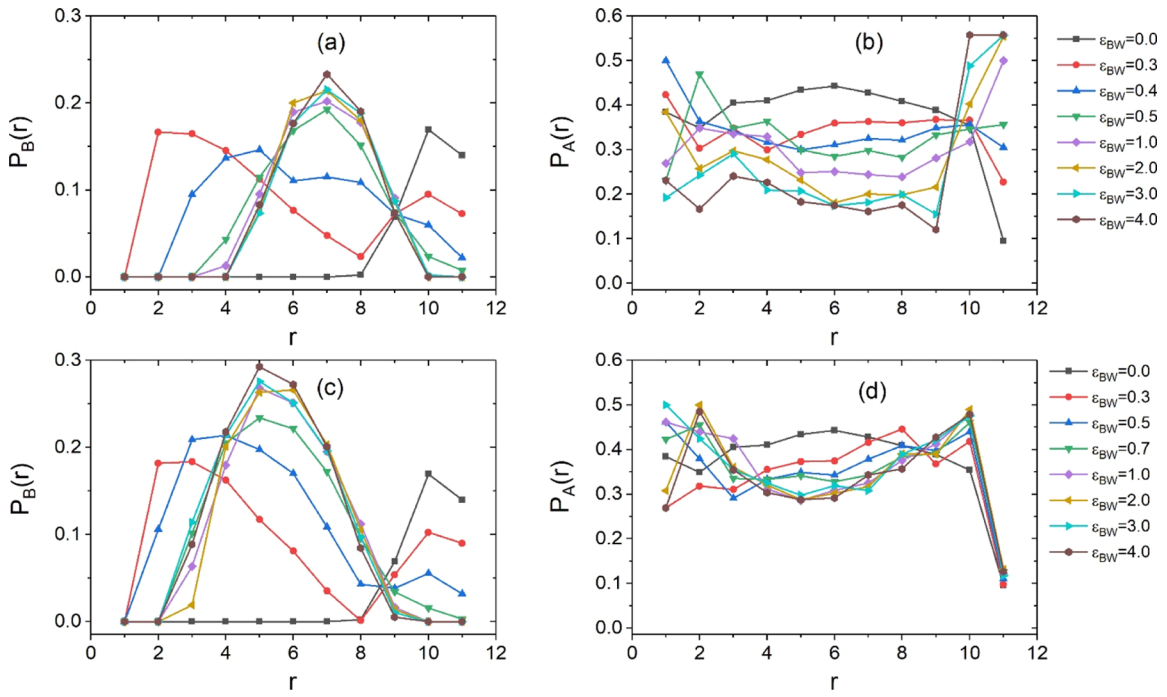

Figure 5. Radial density profiles of A-segments $P_A(r)$ and B-segments $P_B(r)$ in a confining pore of radius $R = 11$. (a,b) Type α case and (c,d) type β case.

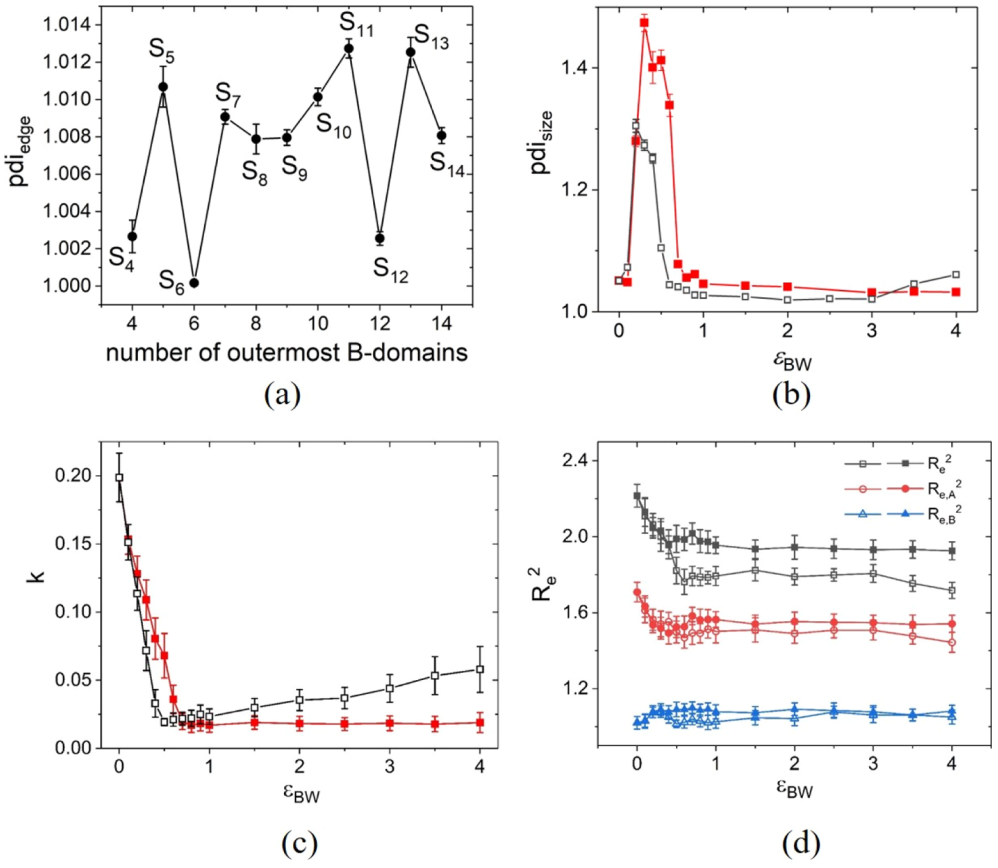

Figure 6. (a) Patch number dependence of the polydispersity index pdi_{edge} of edge length in polyhedrons formed from packing of patches in self-assembled structures S_4−S_{14} shown in Figure 1a,a′. For the self-assembled structures formed at $R = 11$, ε_{BW} dependence of (b) polydispersity index of the size of each B-domain (pdi_{size}), (c) nonsphericity of each B-domain, and (d) normalized mean-square end-to-end distance of AB diblock chains, A-blocks, and B-blocks. Empty and filled symbols correspond to type α and β cases, respectively. Error bars are shown for each data point in the figure.

https://doi.org/10.1021/acs.macromol.2c02166
Macromolecules 2023, 56, 335−348

3.3. Quantitative Information. We calculate some quantities to provide quantitative information on the structures obtained and further explain the observed phase behavior. We calculate the radial density profiles of copolymer segments and estimate the effective pore radius for the B-domains. We calculate the polydispersity index of edge length in the polyhedrons formed by packing of B-domains in the self-assembled structures to elucidate the distribution of B-domains in these structures. Other quantities, including the polydispersity index of the size of each B-domain, nonsphericity of each B-domain, and the normalized mean-square end-to-end distance of AB diblock chains, A-blocks, and B-blocks, are calculated to further provide information on structures and chains.

The above analysis suggests that the effective pore radius for the B-domains should be different in the two types of cases for a given R. We estimate the effective pore radius R_{eff} through calculating the radial density profiles of I-segments $P_I(r)$ (I = A, B) in the confining pore. Figure 5 shows the density profiles of A- and B-segments for systems of R = 11, corresponding to the structures shown in Figure 2. As shown in Figure 5a,c for the two types of cases, a $P_B(r)$ curve has one peak or two peaks corresponding to systems with one category or two categories of B-domains, respectively. For the sake of generality, the effective pore radius R_{eff} for the B-domains is defined as the distance between the peak position of the $P_B(r)$ curve to the pore center. In Figure 5a,c, it is noted that when there is only one category of B-domains and they are away from the pore surface, $R_{eff} \approx 7$ in the type α case when $\varepsilon_{BW} \geq 0.5$, while in the type β case, $R_{eff} \approx 5$ when $\varepsilon_{BW} \geq 0.7$, that is, R_{eff} in the type α case is larger than that in the type β case. This difference is due to the different ε_{AW} values used in the two types of cases. Most of the A-segments are attached to the pore surface due to the attractive interactions between the A-blocks and surface in the type α case when $\varepsilon_{BW} \geq 0.5$, as indicated by the peak at $r = R$ = 11 in $P_A(r)$ curves shown in Figure 5b. Considering the size of a B-domain and the stretching of the solvophilic A-blocks around the B-domain, $R_{eff} \approx 7$ means that the location of the B-domains is quite near the pore surface for a pore of radius 11. However, in the type β case, as shown in Figure 5d, the $P_A(r)$ curve has a small peak at $r = R - 1$ and a much lower value at $r = R$ when $\varepsilon_{BW} \geq 0.7$, indicating that much more solvent molecules than A-segments are located at the pore surface. This is because in the type β case, the pore surface has no energetic preference to the A-segment over solvent as $\varepsilon_{AW} = \varepsilon_{SW} = 0$, while more solvent molecules located at the pore surface can reduce the entropy loss of the polymer. In this case, the peak of the $P_B(r)$ curve is located at $r = R_{eff} \approx 5$, that is, at about the middle point between the pore center and the outermost layer mostly occupied by the solvent, which results in the space being about the same for the A-blocks emitting from a B-domain surface stretching to both the pore center and the pore surface directions.

Figure 6a shows the patch number dependence of the polydispersity index (pdi_{edge}) of edge length in the polyhedrons formed by packing of patches in structures self-assembled inside neutral pores, corresponding to snapshots shown in Figure 1a,a′. From Figure 6a, it is noted that the regular tetrahedron, octahedron, and icosahedron, that is, structures S_4, S_6, and S_{12}, respectively, all have much smaller pdi_{edge} values (in the range 0−0.003). Considering the lattice model used in our simulations, these pdi_{edge} values are quite close to their ideal value of 0. On the other hand, each polyhedron of structures S_5, S_{11}, and S_{13} has a larger pdi_{edge} value than that of its neighbor structures. Hence, the relatively large pdi_{edge} values of polyhedrons from structures S_5, S_{11}, and S_{13} may be the reason that these structures are absent in the phase diagram of type β case and the reason that these structures have relatively small windows in the phase diagram of the type α case. In addition, the relatively large pdi_{edge} value in the polyhedron from structure S_{10} leads to a relatively smaller window of structure S_{10} in the phase diagrams of both type α and β cases. Furthermore, the windows, vacated due to the absence or the relatively smaller windows of structures S_5, S_{10}, S_{11}, and S_{13}, are added to that of their respective neighboring structures (i.e., structures S_4, S_6, S_9, and S_{12}) in the phase diagrams, which further results in the relatively larger window of structures S_4, S_6, S_9, and S_{12} in the phase diagrams. The smaller the pdi_{edge} value, the more uniform the distribution of the B-domains inside the spherical pore. The above results indicate that the system tends to avoid forming polyhedral structures with uneven distribution of B-domains. The reason for the occurrence of structures S_5, S_{11}, and S_{13} in the phase diagram of the type α case is that the number of B-domains should increase continuously to reduce the overstretching of A-blocks as ε_{BW} is increased continuously. Hence, structures with several continuous numbers of B-domains should occur with increasing ε_{BW} at a given R-value in the phase diagram of the type α case, which is the reason that all structures with 1−14 patches occur in the phase diagram of the type α case. This is quite different from that in the type β case. On the other hand, structures S_2 and S_3 are absent in the case of $-\varepsilon_{AW} = \varepsilon_{BW} = 1.0$ due to the structure frustration, as deduced early. It can be deduced that structures S_2 and S_3 are also absent in the phase diagram of the type β case due to the structure frustration. However, in the type α case, structures S_2 and S_3 occur as frequently occurring structures in the phase diagram when $-\varepsilon_{AW} = \varepsilon_{BW} > 1.7$ (as shown in Figure 4a) since in such cases, the entropy loss due to the overcompression of A-blocks in the pattern (2) mentioned above can be offset by the gaining of favorable energy due to the increased contact between A-segments and pore surface (when $-\varepsilon_{AW}$ is large). Hence, the window of structures S_2 and S_3 in the phase diagram of the type α case is relatively small since they are absent due to the structure frustration when ε_{BW} is smaller than 1.7. The windows, vacated due to the absence or the relatively smaller windows of structures S_2 and S_3, are added to that of their respective neighboring structures (S_1 and S_4) in the phase diagrams, which is the reason that structures S_1 and S_4 have a relatively larger window in the phase diagrams of both types of cases. It is interesting to find that the phase diagrams can be well understood based on the variation of the pdi_{edge} curve.

Figure 6b shows the variation in the polydispersity index of the size of each B-domain (pdi_{size}) with ε_{BW}. It is noted that the pdi_{size} curve has a much larger value of ∼1.3 at ε_{BW} = 0.2−0.4 and of 1.3−1.5 at ε_{BW} = 0.2−0.6 for the type α and β cases, respectively. These ε_{BW} regions just correspond to the structures with two categories of B-domains in the system, and the size of each B-domain attached to the pore surface is smaller than that away from the pore surface. In the other ε_{BW} regions, pdi_{size} remains at ∼1.0 and is almost unchanged in the type β case, while in the type α case, it also remains at ∼1.0 almost unchanged at ε_{BW} = 1.0−3.0; however, it increases slightly with ε_{BW} when $\varepsilon_{BW} \geq 3.5$, indicating that the strong A-surface attractions in the type α case can induce a slight difference in the sizes of B-domains.

https://doi.org/10.1021/acs.macromol.2c02166
Macromolecules 2023, 56, 335−348

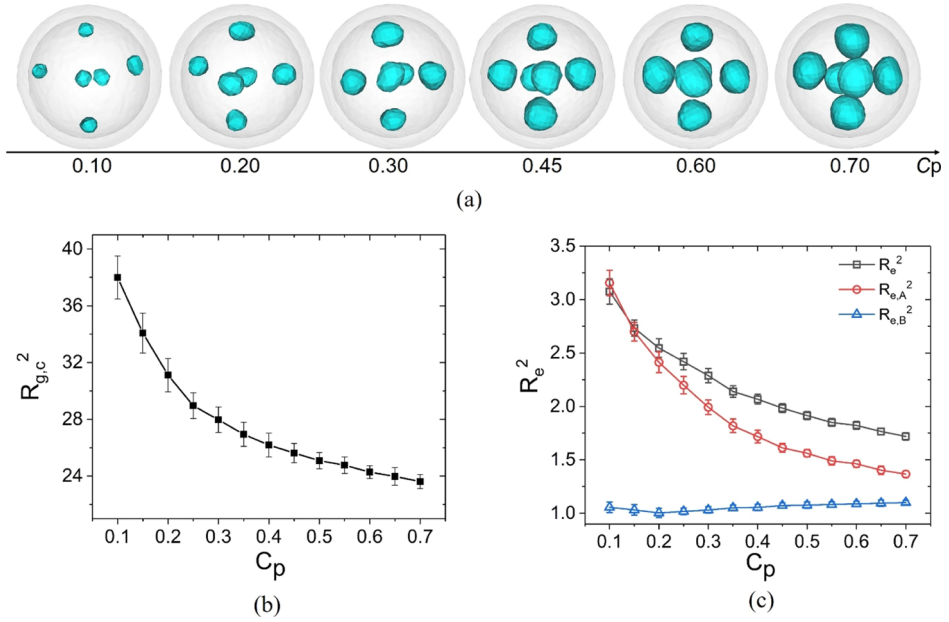

Figure 7. Segment concentration (C_p) dependence of (a) typical snapshots of self-assembled structures, (b) mean-square radius of gyration of the centers of B-domains, and (c) normalized mean-square end-to-end distance of AB diblock chains, A-blocks, and B-blocks, in systems of R = 12 and the block−surface interaction of $-\varepsilon_{AW} = \varepsilon_{BW}$ = 1.0. The spherical B-domains in (a) are shown in blue color.

Figure 6c shows the variation of nonsphericity of each B-domain (κ) with ε_{BW}. It is noted that in both types of cases, the κ curve has a maximum value at ε_{BW} = 0, indicating that the shape of each B-domain is deviating from a sphere. This is because the B-domains are attached to the pore surface and in lens shape at ε_{BW} = 0. With increasing ε_{BW}, each κ curve decreases rapidly until ε_{BW} = 0.5 or 0.7 for the type α and β cases, respectively, where κ reaches a minimum value of ∼0.02. This is because at these small ε_{BW} regions, each system includes two categories of B-domains, lens shaped and nearly spherical, and the proportion of nearly spherical increases with ε_{BW} and becomes 100% at ε_{BW} = 0.5 and 0.7 for the type α and β cases, respectively. With further increasing ε_{BW}, κ remains at the minimum value almost unchanged in the type β case, indicating that the B-domains remain in a nearly spherical shape. In the type α case, however, κ increases slightly with ε_{BW} in the range of ε_{BW} = 1.5−4.0, indicating that the strong A-surface attractions induce a slight deformation of the shape of each B-domain.

Figure 6d shows the variation of the normalized mean-square end-to-end distance of AB diblock chains (R_e^2), A-blocks ($R_{e,A}^2$), and B-blocks ($R_{e,B}^2$), for chains in the self-assembled structures as a function of ε_{BW}. As the length of the B-block is much shorter than that of the A-block, the stretching of the AB chains (characterized byR_e^2) is dominated by the stretching of the A-blocks ($R_{e,A}^2$). This can be clearly seen in Figure 6d where the variations in R_e^2 and $R_{e,A}^2$ are of the same trend. The large value of $R_{e,A}^2(\approx 1.7)$ at ε_{BW} = 0 as shown in Figure 6d indicates that the A-blocks are strongly stretched. This is because when $\varepsilon_{AW} = \varepsilon_{BW}$ = 0, the shorter B-blocks form lens-shaped domains attached to the neutral pore surface, where the A-blocks are only distributed at the inner side of each B-domain, which results in the stretching of A-blocks. With increasing ε_{BW} from 0 to ∼0.5, the stretching of the A-blocks is slightly relieved, as shown in Figure 6d. This is because with increasing ε_{BW}, more and more B-domains are away from the pore surface, and hence, the A-blocks are distributed at all sides of each B-domain, which relieves the stretching of the A-blocks. Upon further increasing ε_{BW}, $R_{e,A}^2$ remains at ∼1.55 and almost unchanged in the type β case, while in the type α case, $R_{e,A}^2$ remains at ∼1.50 till $\varepsilon_{BW} \approx 3$ and decreases slightly upon further increasing ε_{BW}. This is because with the further increase in ε_{BW} in the type α case, the attraction between A-segments and the pore surface increases, and hence, more A-segments are concentrated near the pore surface (density profile is shown in Figure 5b), and the increased number of B-domains with increasing ε_{BW} when $\varepsilon_{BW} \geq 3.5$ (as shown in Figure 4a) can all reduce the stretching of A-blocks.

3.4. Effect of Segment Concentration on the Self-Assembled Structures. Figure 7a shows the variation in typical snapshots of self-assembled structures with the copolymer segment concentration C_p at a fixed pore radius of R = 12 and fixed polymer−surface interactions of $-\varepsilon_{AW} = \varepsilon_{BW}$ = 1.0, and the variation in quantities calculated from these structures with C_p are presented in Figure 7b,c. As shown in Figure 7a, the B-domains are always spherical in shape up to C_p = 0.7 (a value lower than that in the unconfined system where up to C_p = 0.85), and the number of the B-domains keeps six independent of C_p. Figure 7a also shows that the size of each B-domain increases with increasing C_p. The curve in Figure 7b shows the variation in the mean-square radius of gyration of the six B-centers $R_{g,c}^2$ with C_p. The rapid increase in $R_{g,c}^2$ with decreasing C_p indicates that the six B-centers are further away from each other with decreasing C_p. This can be understood based on the following analysis. With decreasing C_p, the number of A-blocks in a system decreases, so the average size of each B-domain decreases as the number of the B-domains is not changed in the system. As the outermost layer of the pore (at $r = R$) is occupied by the A-segment when $-\varepsilon_{AW} = \varepsilon_{BW}$ = 1.0 and the B-domain is close to the A-segments, the distance of each B-center to the pore surface is about the sum of the radius of the B-domain and 1. Hence, the B-centers are gradually close to the pore surface with a decrease in the B-domain size. That is, with decreasing C_p, the B-centers are on a

https://doi.org/10.1021/acs.macromol.2c02166
Macromolecules 2023, 56, 335−348

spherical surface of a gradually large radius; therefore, the mean-square radius of gyration of the six B-centers $R^2_{g,c}$ increases with decreasing C_p. Figure 7c shows that the stretching of AB diblock chains, also dominated by the stretching of the majority of A-blocks as mentioned before, increases rapidly with decreasing C_p. It can be deduced that with decreasing C_p, the A-blocks are more and more swollen by the increased amount of solvent molecules; thus, they tend to be more and more stretched with decreasing C_p.

Our further simulation results show that the number of the B-domains may change little with C_p at other fixed pore radii. Furthermore, varying the volume fraction of one block or the selectivity of the solvent can affect the C_p region for forming spherical structures, just like that observed earlier by Lodge et al.[41] for the unconfined system. Nevertheless, the phase behavior obtained in the present study should be universal as long as the solution system forms spherical structures, regardless of the values of f_B, solvent selectivity, and C_p.

3.5. Comparisons with Related Studies. Our simulation results can be compared with those of related studies. The most related work is the self-assembly of sphere-forming diblock copolymer melts confined in spherical nanopores by Zhao et al.[37] using the self-consistent field theory. The main differences between our system/results and theirs are summarized in the followings. (1) Our model system is in solution state, while theirs is in the melt. (2) We focus on neutral pore surface and surface selective for the majority block, while they focus on pore surface selective to the minority block. (3) Our phase diagrams are constructed by varying the pore radius and the surface−polymer interaction at a fixed volume fraction, while their phase diagram is constructed as a function of the pore radius and the volume fraction of one block at the fixed surface−block interactions. (4) In our phase diagram, each of the structures S_1−S_{14}, being of apparent symmetry, has a window in the type α case, while in the type β case, structures S_2, S_3, S_5, S_{11}, and S_{13} are absent in the phase diagram when $\varepsilon_{BW} > 0$. In their phase diagram, structures S_5 and S_{11} do not have a stable region among the 12 structures of S_1−S_{12} they studied. (5) Structure S_8 is the biaugmented triangular prism belonging to J50 in the Johnson solids in our results, while in their results, it is the triangular dodecahedron belonging to J84 in the Johnson solids. J50 is closer to a sphere compared to that of J84 (which has a larger aspect ratio). J50 was not listed as a candidate structure in their study. On the other hand, J84 is obtained in our study in structure S_{4+4}, which is a structure with two categories of B-domains. (6) We obtained two degenerate structures for structure S_{10}, that is, J17 and J86, while J86 was not listed as a candidate structure for S_{10} in their study. The differences in results between theirs and ours should be mainly due to the differences in model/parameters in differences (1−3) summarized above. Another important factor that may result in differences between their results and ours is the fluctuation of the system, which is considered automatically in our simulations but has been neglected in the self-consistent field theory calculation. Fluctuation is more important in a solution-state system than in a melt system. On the other hand, some similar results are found between theirs and ours, for example, the five structures S_1, S_4, S_6, S_9, and S_{12} have much larger windows in the phase diagram than others. This supports our conclusion that the system tends to avoid forming polyhedral structures with uneven distribution of solvophobic domains. In addition, their study showed that the stability order of the three candidate structures (triangular dodecahedron, anticube, and cube) for S_8 is triangular dodecahedron > anticube > cube, which supports our conclusion that the system prefers structures with all/more triangular faces so that the shape of the structure is closer to a sphere.

Other related studies include the experimental/simulation studies of self-assembly of diblock copolymers under emulsion solvent−evaporation-induced 3D soft confinement.[31−36] The packing of patches in ref 31 is similar to that obtained in our simulations for small particles with the number of patches being N_p = 2−6; however, low symmetry occurs when N_p = 5 even in simulation results of that study.[31] Bigger particles obtained in that study[31] are of raspberry-like structures. This difference should be mainly due to the difference in confinement, which is hard in our study while soft in ref 31, and solvent evaporation in that study results in the low symmetry of patches. Another type of related studies are studies of packing of microsphere[39]/nanoparticle[40] clusters under 3D soft confinement or unconfined Lennard−Jones (LJ) clusters[54,55] and metal (Sutton−Chen) clusters.[55,56] The packing of spherical particles in these studies[39,40,54−56] is the same as that of patches in our simulations when particle number is N_p = 3−7 and N_p = 13, while discrepancies appear when N_p = 8−12 and N_p = 14−15.[39,54−56] Especially, the structures from these LJ or metal (Sutton−Chen) clusters are mostly nonconvex when N_p = 8−15, except for the icosahedron. The structures with $7 < N_p < 20$ roughly follow an essentially icosahedral growth scheme, with the structures either assembling en route to or growing onto an icosahedral cluster (N_p = 13).[57] The B-domains in our study are dispersed in the matrix of solvophilic A-blocks and solvent, where the entropy of the chains plays an important role in affecting the packing of B-domains and leads to uniform B-domains distribution in the confined space. This is the reason that polyhedrons packed by the B-domains of up to 14 are in apparent symmetry in our study.

4. CONCLUSIONS

Self-assembly of sphere-forming solution-state amphiphilic AB diblock copolymers confined in a spherical nanopore is studied using a simulated annealing technique. Two types of cases of different pore−surface/copolymer interactions are studied: (α) the surface being neutral to the two blocks ($\varepsilon_{AW} = \varepsilon_{BW} = 0$) or attractive to the solvophilic A-blocks and simultaneously repulsive to the solvophobic B-blocks, that is, $-\varepsilon_{AW} = \varepsilon_{BW} > 0$; and ($\beta$) the surface being neutral to the two blocks or repulsive to B-blocks, that is, $\varepsilon_{BW} \geq 0$, while $\varepsilon_{AW} = 0$ remains unchanged. Phase diagrams are constructed as a function of the pore radius R and the interaction parameter ε_{BW}. Nanospheres with various numbers of B-domains are obtained and named S_i or S_{i+j}, with i and j being the number of B-domains located at the outermost layer and the inner layer of the confining pore, respectively. Quantitative calculations are performed to elucidate the mechanisms of window size of nanospheres with different numbers of patches in the phase diagrams and the structure details. It is found that each B-domain is nearly spherical in shape in all cases, except in the case of neutral or nearly neutral surfaces where each patch is in a lens shape. Polyhedrons formed by the packing of the i patches in structures S_i and S_{i+1} are usually with high symmetry when $4 \leq i \leq 14$, and especially, three Platonic solids and seven Johnson solids are identified among them. Furthermore, these polyhedral structures only depend on the number of patches,

https://doi.org/10.1021/acs.macromol.2c02166
Macromolecules 2023, 56, 335−348

not on the domain shape or on whether the structure is S_i or S_{i+1}. Each polyhedral structure has all or most of its faces in a triangular shape, such as the three identified Platonic solids, a regular tetrahedron (S_4), an octahedron (S_6), and an icosahedron (S_{12}), are all composed of triangular faces, and the seven Johnson solids identified in our simulations have all (J12, J13, J17, and J51) or most of their faces (except only one or two tetragonal faces in J50 and J87, or J86, respectively) in triangular shape, which brings the shape of the polyhedron being closer to a sphere. Depending on R, structures S_1, S_4, S_6, S_9, and S_{12} occur in the whole ε_{BW} range and have relatively larger windows in the phase diagrams in both types of cases. Each of structures S_1−S_{14} has a window in the phase diagram of type α case, while in the type β case, structures S_2, S_3, S_5, S_{11}, and S_{13} are absent in the phase diagram when $\varepsilon_{BW} > 0$. It can be deduced that in the type β case, the structure frustration should be the reason leading to the absence of structures S_2 and S_3 in the phase diagram, while the relatively larger polydispersity index of the edge length in the respective polyhedrons should be the reason leading to the absence of structures S_5, S_{11}, and S_{13}, and the relatively smaller window of structure S_{10}, in the phase diagram of type β case. The above-mentioned reasons for the type β case lead to relatively smaller windows of structures S_2, S_3, S_5, S_{10}, S_{11}, and S_{13} in the phase diagram of the type α case. The windows, vacated due to the absence or the relatively smaller windows of structures S_2, S_3, S_5, S_{10}, S_{11}, and S_{13}, are added to that of their respective neighboring structures (i.e., structures S_1, S_4, S_6, S_9, and S_{12}), which further results in the relatively larger windows of these neighboring structures in the phase diagrams. At a fixed pore radius R, a nonmonotonic change in the number of B-domains with ε_{BW} is observed in the type α case. However, in the type β case, this number remains almost unchanged with increasing ε_{BW} in systems with only one category of B-domains (when $\varepsilon_{BW} \geq 0.7$). Structures S_{i+j} (with two categories of B-domains) are observed when ε_{BW} is relatively small, and polyhedrons formed by packing the $i + j$ B-domains in structures S_{i+j} (with $j > 1$) usually have no apparent symmetry in both type of α and β cases. An exception is that J84, the eighth Johnson solid identified in our study, is observed by packing the eight B-domains in structure S_{4+4}. Our study also shows that at a given R, the effective pore radius of the B-domains in the type β case is smaller than that in the type α case when $\varepsilon_{BW} \geq 0.7$. The size of each B-domain is uniform in systems with only one category of B-domains. Furthermore, the solvophilic A-blocks have a larger stretching when all the B-domains are attached to the pore surface in the case of a neutral pore or when the segment concentration of the system is low.

The phase sequence obtained in the present solution-state system is consistent with that obtained previously in the melt system while some differences exist. The differences should be mainly due to the differences in model/parameters used between the two studies. The phase sequence obtained in our simulations is also compared with that obtained in other related systems. The phase behavior obtained in the present study should be universal as long as the solution-state system forms spherical structures or spherical micelles, regardless of the copolymer composition and concentration, as well as solvent selectivity. Besides, patchy nanospheres obtained in our system can be well controlled in several aspects, such as the size and shape of a patch, and the distance between two neighboring patches can be controlled by varying the chain length of the block copolymer or that of A- or B-blocks, the concentration of the solution and the interaction between the two blocks. Our simulation results may provide guidelines for understanding nanospheres with polyhedral shaped structures from self-assembly of amphiphilic block copolymer solutions.

AUTHOR INFORMATION

Corresponding Authors

Yao Li − *School of Physics and Key Laboratory of Functional Polymer Materials of Ministry of Education, Nankai University, and Collaborative Innovation Center of Chemical Science and Engineering, Tianjin 300071, China*; Email: liyao@nankai.edu.cn

Baohui Li − *School of Physics and Key Laboratory of Functional Polymer Materials of Ministry of Education, Nankai University, and Collaborative Innovation Center of Chemical Science and Engineering, Tianjin 300071, China*; orcid.org/0000-0002-8403-1220; Email: baohui@nankai.edu.cn

Authors

Jiaping Wu − *School of Physics and Key Laboratory of Functional Polymer Materials of Ministry of Education, Nankai University, and Collaborative Innovation Center of Chemical Science and Engineering, Tianjin 300071, China*

Xin Wang − *School of Physics and Key Laboratory of Functional Polymer Materials of Ministry of Education, Nankai University, and Collaborative Innovation Center of Chemical Science and Engineering, Tianjin 300071, China*

Zheng Wang − *School of Physics and Key Laboratory of Functional Polymer Materials of Ministry of Education, Nankai University, and Collaborative Innovation Center of Chemical Science and Engineering, Tianjin 300071, China*

Yuhua Yin − *School of Physics and Key Laboratory of Functional Polymer Materials of Ministry of Education, Nankai University, and Collaborative Innovation Center of Chemical Science and Engineering, Tianjin 300071, China*; orcid.org/0000-0003-1962-8167

Run Jiang − *School of Physics and Key Laboratory of Functional Polymer Materials of Ministry of Education, Nankai University, and Collaborative Innovation Center of Chemical Science and Engineering, Tianjin 300071, China*

Complete contact information is available at: https://pubs.acs.org/10.1021/acs.macromol.2c02166

Notes

The authors declare no competing financial interest.

ACKNOWLEDGMENTS

This work was supported by the National Natural Science Foundation of China (21829301, 21774066, and 22173051), Fundamental Research Funds for the Central Universities, Nankai University (63221053), and Startup Funds for scholars of the Nankai University. The authors would like to thank the corresponding Committees for their financial support.

REFERENCES

(1) Bates, F. S.; Fredrickson, G. H. Block Copolymers—Designer Soft Materials. *Phys. Today* **1999**, *52*, 32.

(2) Hamley, I. W.*The Physics of Block Copolymers*; Oxford University Press: Oxford, U.K., 1998.

(3) Russell, T. P.; Chai, Y. 50th Anniversary Perspective: Putting the Squeeze on Polymers: A Perspective on Polymer Thin Films and Interfaces. *Macromolecules* **2017**, *50*, 4597−4609.

(4) Schacher, F. H.; Rupar, P. A.; Manners, I. Functional Block Copolymers: Nanostructured Materials with Emerging Applications. *Angew. Chem., Int. Ed.* **2012**, *51*, 7898−7921.
(5) Shi, A. C.; Li, B. Self-Assembly of Diblock Copolymers under Confinement. *Soft Matter* **2013**, *9*, 1398−1413.
(6) Shin, J. J.; Kim, E. J.; Ku, K. H.; Lee, Y. J.; Hawker, C. J.; Kim, B. J. 100th Anniversary of Macromolecular Science Viewpoint: Block Copolymer Particles: Tuning Shape, Interfaces, and Morphology. *ACS Macro Lett.* **2020**, *9*, 306−317.
(7) Fasolka, M. J.; Mayes, A. M. Block Copolymer Thin Films: Physics and Applications. *Annu. Rev. Mater. Res.* **2001**, *31*, 323−355.
(8) Segalman, R. A. Patterning with Block Copolymer Thin Films. *Mater. Sci. Eng., R* **2005**, *48*, 191−226.
(9) Cheng, J. Y.; Ross, C. A.; Smith, H. I.; Thomas, E. L. Templated Self-Assembly of Block Copolymers: Top-down Helps Bottom-Up. *Adv. Mater.* **2006**, *18*, 2505−2521.
(10) Albert, J. N. L.; Epps, T. H. Self-Assembly of Block Copolymer Thin Films. *Mater. Today* **2010**, *13*, 24−33.
(11) Ok, S.; Vayer, M.; Sinturel, C. A decade of innovation and progress in understanding the morphology and structure of heterogeneous polymers in rigid confinement. *Soft Matter* **2021**, *17*, 7430.
(12) Wu, Y.; Cheng, G.; Katsov, K.; Sides, S. W.; Wang, J.; Tang, J.; Fredrickson, G. H.; Moskovits, M.; Stucky, G. D. Composite Mesostructures by Nano-Confinement. *Nat. Mater.* **2004**, *3*, 816−822.
(13) Kalra, V.; Mendez, S.; Lee, J. H.; Nguyen, H.; Marquez, M.; Joo, Y. L. Confined Assembly in Coaxially Electrospun Block-Copolymer Fibers. *Adv. Mater.* **2006**, *18*, 3299−3303.
(14) Ma, M.; Krikorian, V.; Yu, J. H.; Thomas, E. L.; Rutledge, G. C. Electrospun Polymer Nanofibers with Internal Periodic Structure Obtained by Microphase Separation of Cylindrically Confined Block Copolymers. *Nano Lett.* **2006**, *6*, 2969−2972.
(15) Dobriyal, P.; Xiang, H.; Kazuyuki, M.; Chen, J. T.; Jinnai, H.; Russell, T. P. Cylindrically Confined Diblock Copolymers. *Macromolecules* **2009**, *42*, 9082−9088.
(16) Wu, Y.; Livneh, T.; Zhang, Y. X.; Cheng, G.; Wang, J.; Tang, J.; Moskovits, M.; Stucky, G. D. Templated Synthesis of Highly Ordered Mesostructured Nanowires and Nanowire Arrays. *Nano Lett.* **2004**, *4*, 2337−2342.
(17) Arsenault, A. C.; Rider, D. A.; Tétreault, N.; Chen, J. I. L.; Coombs, N.; Ozin, G. A.; Manners, I. Block Copolymers under Periodic, Strong Three-Dimensional Confinement. *J. Am. Chem. Soc.* **2005**, *127*, 9954−9955.
(18) Rider, D. A.; Chen, J. I. L.; Eloi, J. C.; Arsenault, A. C.; Russell, T. P.; Ozin, G. A.; Manners, I. Controlling the Morphologies of Organometallic Block Copolymers in the 3-Dimensional Spatial Confinement of Colloidal and Inverse Colloidal Crystals. *Macromolecules* **2008**, *41*, 2250−2259.
(19) Wyman, I.; Njikang, G.; Liu, G. When Emulsification Meets Self-Assembly: The Role of Emulsification in Directing Block Copolymer Assembly. *Prog. Polym. Sci.* **2011**, *36*, 1152−1183.
(20) Higuchi, T.; Tajima, A.; Motoyoshi, K.; Yabu, H.; Shimomura, M. Frustrated Phases of Block Copolymers in Nanoparticles. *Angew. Chem., Int. Ed.* **2008**, *47*, 8044−8046.
(21) Li, L.; Matsunaga, K.; Zhu, J.; Higuchi, T.; Yabu, H.; Shimomura, M.; Jinnai, H.; Hayward, R. C.; Russell, T. P. Solvent-Driven Evolution of Block Copolymer Morphology under 3D Confinement. *Macromolecules* **2010**, *43*, 7807−7812.
(22) Wang, Q.; Yan, Q.; Nealey, P. F.; de Pablo, J. J. Monte Carlo simulations of diblock copolymer thin films confined between two homogeneous surfaces. *J. Chem. Phys.* **2000**, *112*, 450−464.
(23) Wang, Q.; Nealey, P. F.; de Pablo, J. J. Monte Carlo Simulations of Asymmetric Diblock Copolymer Thin Films Confined between Two Homogeneous Surfaces. *Macromolecules* **2001**, *34*, 3458−3470.
(24) Reffner, J. R.The Influence of Surfaces on Structure Formation: I. Artificial Epitaxy of Metals on Polymers. II. Phase Separation of Block Copolymers and Polymer Blends under Nonplanar Surface Constraints. Ph.D. Thesis, Univ. Massachusetts Amherst, 1992.
(25) Yabu, H.; Higuchi, T.; Shimomura, M. Unique Phase-Separation Structures of Block-Copolymer Nanoparticles. *Adv. Mater.* **2005**, *17*, 2062−2065.
(26) He, X.; Song, M.; Liang, H.; Pan, C. Self-Assembly of the Symmetric Diblock Copolymer in a Confined State : Monte Carlo Simulation. *J. Chem. Phys.* **2001**, *114*, 10510.
(27) Yu, B.; Li, B.; Jin, Q.; Ding, D.; Shi, A. Self-Assembly of Symmetric Diblock Copolymers Confined in Spherical Nanopores. *Macromolecules* **2007**, *40*, 9133−9142.
(28) Yu, B.; Sun, P.; Chen, T.; Jin, Q.; Ding, D.; Li, B.; Shi, A.-C. Confinement-Induced Novel Morphologies of Block Copolymers. *Phys. Rev. Lett.* **2006**, *96*, 138306.
(29) Li, W.; Wickham, R. A.; Garbary, R. A. Phase Diagram for a Diblock Copolymer Melt under Cylindrical Confinement. *Macromolecules* **2006**, *39*, 806−811.
(30) Wang, Y.; Qin, Y.; Berger, A.; Yau, E.; He, C.; Zhang, L.; Gösele, U.; Knez, M.; Steinhart, M. Nanoscopic Morphologies in Block Copolymer Nanorods as Templates for Atomic-Layer Deposition of Semiconductors. *Adv. Mater.* **2009**, *21*, 2763−2766.
(31) Deng, R.; Li, H.; Liang, F.; Zhu, J.; Li, B.; Xie, X.; Yang, Z. Soft Colloidal Molecules with Tunable Geometry by 3D Confined Assembly of Block Copolymers. *Macromolecules* **2015**, *48*, 5855−5860.
(32) Deng, R.; Zheng, L.; Mao, X.; Li, B.; Zhu, J. Transformable Colloidal Polymer Particles with Ordered Internal Structures. *Small* **2021**, *17*, 2006132.
(33) Kim, M. P.; Kang, D. J.; Jung, D. W.; Kannan, A. G.; Kim, K. H.; Ku, K. H.; Jang, S. G.; Chae, W. S.; Yi, G. R.; Kim, B. J. Gold-Decorated Block Copolymer Microspheres with Controlled Surface Nanostructures. *ACS Nano* **2012**, *6*, 2750−2757.
(34) Deng, R.; Liu, S.; Li, J.; Liao, Y.; Tao, J.; Zhu, J. Mesoporous Block Copolymer Nanoparticles with Tailored Structures by Hydrogen-Bonding-Assisted Self-Assembly. *Adv. Mater.* **2012**, *24*, 1889−1893.
(35) Deng, R.; Liang, F.; Qu, X.; Wang, Q.; Zhu, J.; Yang, Z. Diblock Copolymer Based Janus Nanoparticles. *Macromolecules* **2015**, *48*, 750−755.
(36) Mao, X.; Li, H.; Kim, J.; Deng, S.; Deng, R.; Kim, B. J.; Zhu, J. Polymersome Formation by Solvent Annealing-Induced Structural Reengineering under 3D Soft Confinement. *Nano Res.* **2021**, *14*, 4644−4649.
(37) Zhao, F.; Xu, Z.; Li, W. Self-Assembly of Asymmetric Diblock Copolymers under the Spherical Confinement. *Macromolecules* **2021**, *54*, 11351−11359.
(38) Conway, J. H.; Sloane, N. J. A.*Sphere Packings, Lattices and Groups*; Springer: New York, 1999.
(39) Manoharan, V. N.; Elsesser, M. T.; Pine, D. J. Dense Packing and Symmetry in Small Clusters of Microspheres. *Science* **2003**, *301*, 483−487.
(40) Zhang, Z.; Xia, Y.; Wan, S.; Yang, D.; Dong, A. Confinement Assembly in Polymeric Micelles Enables Nanoparticle Superstructures with Tunable Molecular-Like Geometries. *Small Methods* **2022**, *6*, 2200014.
(41) Lodge, T. P.; Pudil, B.; Hanley, K. J. The Full Phase Behavior for Block Copolymers in Solvents of Varying Selectivity. *Macromolecules* **2002**, *35*, 4707−4717.
(42) Thomas, A.; Schierhorn, M.; Wu, Y.; Stucky, G. Assembly of Spherical Micelles in 2D Physical Confinements and Their Replication into Mesoporous Silica Nanorods. *J. Mater. Chem.* **2007**, *17*, 4558−4562.
(43) Larson, R. G. Self-Assembly of Surfactant Liquid Crystalline Phases by Monte Carlo Simulation. *J. Chem. Phys.* **1989**, *91*, 2479−2488.
(44) Larson, R. G. Monte Carlo Simulation of Microstructural Transitions in Surfactant Systems. *J. Chem. Phys.* **1992**, *96*, 7904−7918.

https://doi.org/10.1021/acs.macromol.2c02166
Macromolecules 2023, 56, 335−348

(45) Carmesin, C.; Kremer, K. The Bond Fluctuation Method: A New Effective Algorithm for the Dynamics of Polymers in All Spatial Dimensions. *Macromolecules* **1988**, *21*, 2819−2823.
(46) Kirkpatrick, S.; Gelatt, C. D., Jr.; Vecchi, M. P. Optimization by Simulated Annealing. *Science* **1983**, *220*, 671−680.
(47) Grest, G. S.; Soukoulis, C. M.; Levin, K. Cooling-Rate Dependence for the Spin-Glass Ground-State Energy: Implications for Optimization by Simulated Annealing. *Phys. Rev. Lett.* **1986**, *56*, 1148−1151.
(48) Sun, P.; Yin, Y.; Li, B.; Chen, T.; Jin, Q.; Ding, D.; Shi, A. C. Simulated Annealing Study of Morphological Transitions of Diblock Copolymers in Solution. *J. Chem. Phys.* **2005**, *122*, 204905.
(49) Theodorou, D. N.; Suter, U. W. Shape of Unperturbed Linear Polymers: Polypropylene. *Macromolecules* **1985**, *18*, 1206−1214.
(50) Mattice, W. L.; Suter, U. W.*Conformational Theory of Large Molecules: The Rotational Isomeric State Model in Macromolecular Systems*; Wiley-Interscience, 1994.
(51) Berezkin, A. V.; Papadakis, C. M.; Potemkin, I. I. Vertical Domain Orientation in Cylinder-Forming Diblock Copolymer Films upon Solvent Vapor Annealing. *Macromolecules* **2016**, *49*, 415−424.
(52) Wenninger, M. J.*Polyhedron Models*; Cambridge University Press, 1974..
(53) Johnson, N. W. Convex Polyhedra with Regular Faces. *Can. J. Math.* **1966**, *18*, 169−200.
(54) Wales, D. J.; Doye, J. P. K. Global Optimization by Basin-Hopping and the Lowest Energy Structures of Lennard-Jones Clusters Containing up to 110 Atoms. *J. Phys. Chem. A* **1997**, *101*, 5111−5116.
(55) Wales, D. J.; Doye, J. P. K.; Dullweber, A.; Hodges, M. P.; Calvo, F. Y. N. F.; Hernández-Rojas, J.; Middleton, T. F.The Cambridge Cluster Database. http://www-wales.ch.cam.ac.uk/CCD.html (accessed August 18, 2013).
(56) Doye, J. P. K.; Wales, D. J. Global Minima for Transition Metal Clusters Described by Sutton-Chen Potentials. *New J. Chem.* **1998**, *22*, 733−744.
(57) Urban, A. S.; Shen, X.; Wang, Y.; Large, N.; Wang, H.; Knight, M. W.; Nordlander, P.; Chen, H.; Halas, N. J. Three-Dimensional Plasmonic Nanoclusters. *Nano Lett.* **2013**, *13*, 4399−4403.

https://doi.org/10.1021/acs.macromol.2c02166
Macromolecules 2023, 56, 335−348